Volume 25
Number 48
28 December 2023
Pages 32731–33204

PCCP

Physical Chemistry Chemical Physics

rsc.li/pccp

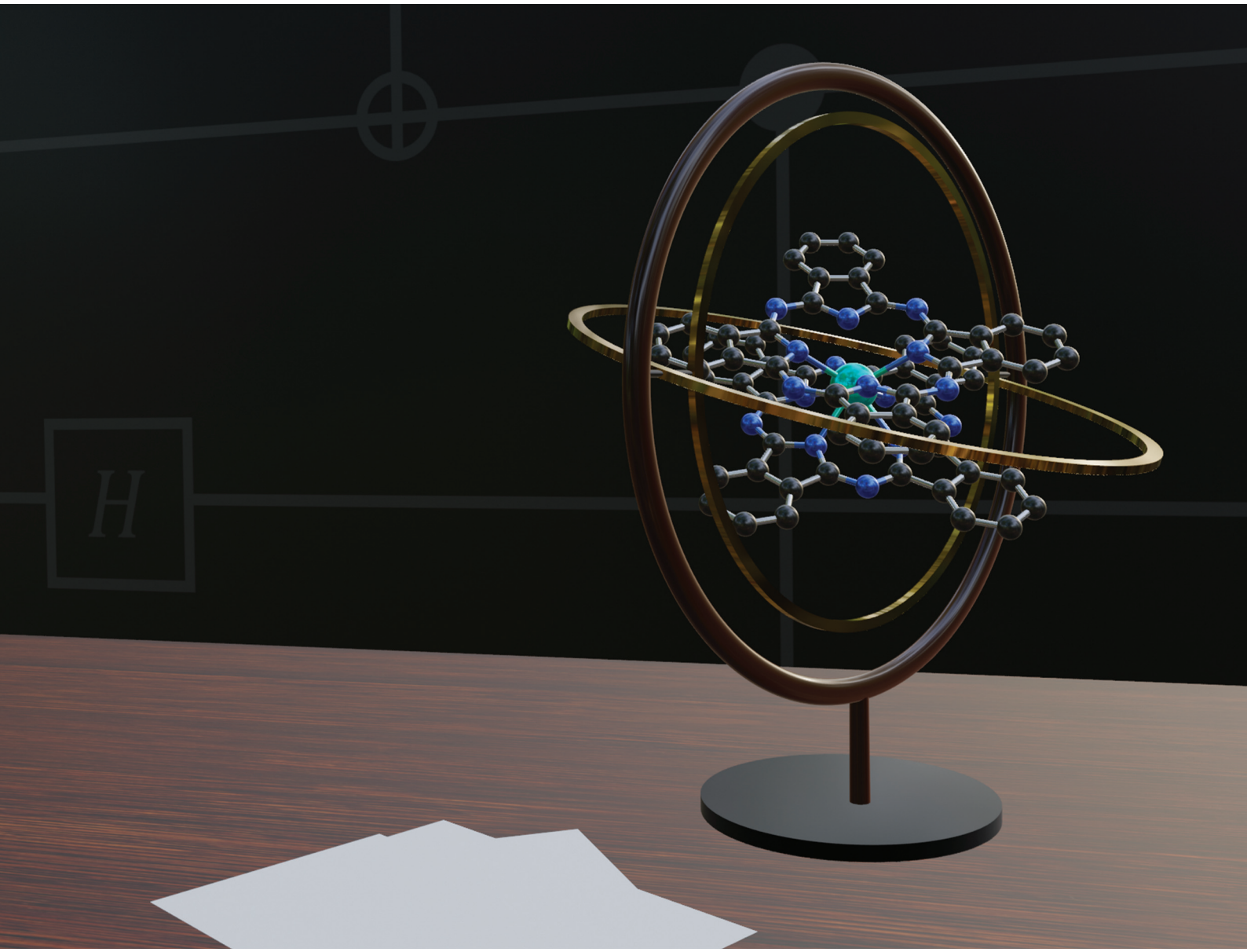

ISSN 1463-9076

ROYAL SOCIETY OF CHEMISTRY

PAPER

Kieran Hymas and Alessandro Soncini
Triggering single-molecule qubit spin dynamics *via* non-Abelian geometric phase effects

PCCP Owner Societies

PCCP

PAPER

View Article Online
View Journal | View Issue

Cite this: *Phys. Chem. Chem. Phys.*, 2023, **25**, 32813

Triggering single-molecule qubit spin dynamics *via* non-Abelian geometric phase effects†

Kieran Hymas [a] and Alessandro Soncini *[b]

We illustrate how macroscopic rotations can be utilised to trigger and control a spin dynamics within the ground doublet of both Kramers and non-Kramers-type molecular nanomagnets *via* the non-Abelian character of the time-evolution operator. For Kramers magnets, we show how this effect can be harnessed to realise single-qubit quantum gates and give the explicit example of a recently reported $CoCl_2(tu)_4$ single-molecule magnet (SMM). We demonstrate that gating operations could be performed on this magnet in as fast as 10 ps before the breakdown of adiabaticity, much faster than typical spin–lattice relaxation times. Based on this effect, we also suggest $CoCl_2(tu)_4$ as a quantum gyroscope for sensing yaw-axis rotations. For integer spin nanomagnets where non-axial crystal field interactions often lift ground state degeneracy, we show how spin dynamics from the non-Abelian geometric propagator can be recovered using non-adiabatic macroscopic rotations not-necessarily resonant with the tunnel splitting gap. Using the well-known $TbPc_2$ single-ion magnet as a further example, we identify an experimentally plausible non-adiabatic rotation that induces a coherent superposition of tunnelling ground states, tantamount to preparing each member of a $TbPc_2$ ensemble in the maximal angular momentum state $|m_J = 6\rangle$. The detection of an ensuing coherent oscillation of the macroscopic magnetisation polarised along the $TbPc_2$ principal magnetic axis after the completed rotation could then proceed *via* time-resolved magnetisation measurements.

Received 24th June 2023,
Accepted 23rd September 2023

DOI: 10.1039/d3cp02939e

rsc.li/pccp

1 Introduction

The rich physics underpinning single-molecule superparamagnetism has been intensely studied since the discovery of single-molecule magnets (SMMs) in 1993[1] with a mind towards their application as microscopic units in molecular memory devices[2–4] and novel quantum information technologies.[5–9] While the coherent and incoherent dynamics which result in 'under-the-barrier' fast magnetic relaxation has foiled current attempts at room temperature single-molecule magnet memory,[10–14] these dynamical processes can instead be harnessed for the manipulation of single-molecule magnet qubit states. Generally, quantum logic gates are implemented in these systems *via* the application of an external resonant microwave or radio-frequency radiation that coherently prepares the nanomagnet in superpositions of energy eigenstates which oscillate in time when the radiation is switched off.[15–17] The time-evolution of these linear combinations is then detectable as Rabi oscillations in time-resolved spin-echo[18,19] or non-equilibrium electrical current[20] measurements subject to decoherence from the local environment of the qubit. Two-qubit quantum logic gates (*e.g.* CNOT and $\sqrt{\text{iSWAP}}$) have also been implemented in coupled paramagnetic qubit architectures *via* *g*-factor engineering of lanthanide ions[21] and modular supramolecular linkers in paramagnetic rings.[22,23] Addressing individual qubits in linked vanadyl–porphyrin dimers has also recently been reported by taking advantage of a weak intramolecular exchange coupling and small homogeneous linewidths intrinsic to the molecule.[24]

In 1984, Wilczek and Zee showed that the adiabatic transport of a quantum system around a closed path in Hamiltonian parameter space can induce a coherent dynamics between energy eigenstates of a degenerate manifold owing to an emergent non-Abelian gauge structure in the geometric component of the time evolution operator.[25] This opened the door for holonomic quantum computation where gating operations correspond to the transport of a degenerate eigenspace (the holonomic qubit computational basis) along holonomies in parameter space.[26] When the space of cyclically evolving parameters coincides with the coordinates of real space (*e.g.* macroscopic rotations), a connection between the Hilbert space of the quantum system and the geometry of the physical space which it occupies, is clearly established. The potential for rotation-induced non-Abelian dynamics in easy-plane Kramers-type spin

[a] *Commonwealth Scientific and Industrial Research Organisation (CSIRO), Clayton, Victoria 3168, Australia. E-mail: kieran.hymas@csiro.au*
[b] *Department of Chemical Sciences, University of Padova, Via Marzolo 1, 35131 Padova, Italy. E-mail: alessandro.soncini@unipd.it*

† Electronic supplementary information (ESI) available: Derivation of the non-adiabatic non-Abelian Berry phase; effect of crystal field lowering and hyperfine coupling in $TbPc_2$. See DOI: https://doi.org/10.1039/d3cp02939e

systems (where time-reversal symmetry enforces an exact ground state degeneracy in the absence of external magnetic perturbations) was first exposed by Zee.[27] In that work he pinpointed a mechanism for rotation-induced frequency splitting of nuclear quadrupole resonance spectra obtained for a $I = 3/2$ ^{35}Cl nuclear spin.[28]

Geometric phase effects have previously been suggested as mechanisms to trigger and control the coherent dynamics of single-molecule magnets[29–31] and related spin systems.[32–35] As the electronic spin of the SMM adiabatically follows the rotating crystal field potential it can accumulate a non-Abelian geometric phase during the cyclic rotation. Similarly, the generation of a coherent spin dynamics *via* macroscopic rotations was suggested for ensembles of nitrogen-vacancy (NV) centres where a longitudinal magnetic field (rotating simultaneously with the NV centre quantisation axis) was proposed to enforce degeneracy.[36] While largely successful as potential qubits and gyroscopes, NV centres lack the synthetic customisability of molecular nanomagnets. Since the rotation-induced spin dynamics of a SMM is strongly correlated with the microscopic parameters of its associated spin Hamiltonian (*vide infra*) this offers a bottom-up synthetic pathway to tune geometric effects in SMMs for applications such as holonomic quantum computation and inertial sensing.

In this manuscript we show how macroscopic rotations can trigger a spin dynamics in the degenerate or quasi-degenerate ground doublet of Kramers and non-Kramers molecular nanomagnets, respectively, *via* the non-Abelian character of their time-evolution operator. We first discuss the sensitivity of the non-Abelian Berry phase to the effective crystal field parameters and, with representative examples for each nanomagnet class, we construct single-qubit Hadamard quantum logic gates using specific rotation paths. In non-Kramers magnets, where non-axial terms in the crystal field Hamiltonian are poised to remove ground state degeneracy through a tunnel splitting between the otherwise bistable ground states, we recover a non-Abelian time evolution operator for the quasi-degenerate ground doublet by relaxing the stringent requirement of adiabatic rotation. In this case, we derive an analytical relationship between the rotation time and rotation axis canting angle which leads to the realisation of all possible Hadamard gates with the tunnelling ground doublet acting as a computational basis. We finally discuss the detection of this effect *via* the resultant collective magnetic moment oscillation of the non-Kramers nanomagnet crystal.

2 Theoretical model

2.1 Nanomagnet effective spin Hamiltonian

The microscopic origin of magnetic anisotropy in SMMs results from the interplay between electrostatic crystal field effects and spin–orbit coupling mainly affecting the electronic states of the paramagnetic ions' 3d or 4f unpaired electrons. In polynuclear nanomagnets, intramolecular spin–spin interactions can too influence the overall magnetic anisotropy. For most non-lanthanide SMMs, the effective spin Hamiltonian $H_S = DS_z^2 + E(S_x^2 - S_y^2)$ is often a good starting point to describe the zero-field splitting of orbital angular momentum quenched magnetic levels within a given ground manifold $^{2S+1}\Gamma_0$.[37] The first term of H_S accounts for an axial magnetic anisotropy of the electronic spin $\mathbf{S} = (S_x, S_y, S_z)$ and is always negative for single-molecule magnets. The second term accounts for rhombic magnetic anisotropy and, when S_z is quantised along the principal magnetic axis, we have that $0 \leq E < D/3$. We utilise the aforementioned effective spin Hamiltonian throughout this manuscript except in Section 3.5 where the example of a rotating lanthanide single-ion magnet necessitates the inclusion of higher-order irreducible tensor operators into the effective spin Hamiltonian.

In the laboratory frame, the Hamiltonian for the rotating system takes the form $H(\alpha, \beta, \gamma) = \mathscr{R}(\alpha, \beta, \gamma)H_S\,\mathscr{R}^\dagger(\alpha, \beta, \gamma)$ where the rotation operator

$$\mathscr{R}(\alpha, \beta, \gamma) = e^{-i\alpha S_z}e^{-i\beta S_y}e^{-i\gamma S_z} \quad (1)$$

is parametrised by the Euler angles α, β and γ.[38] The instantaneous energy eigenstates $|\eta_a(\alpha, \beta, \gamma)\rangle$ of the rotated Hamiltonian $H(\alpha, \beta, \gamma)$ are constructed from rotations of the eigenstates $|\phi_a\rangle$ of H_S using the operator $\mathscr{R}(\alpha, \beta, \gamma)$.[27] It is thus simple to show that $H(\alpha, \beta, \gamma)\,|\eta_a(\alpha, \beta, \gamma)\rangle = \varepsilon_a|\eta_a(\alpha, \beta, \gamma)\rangle$ where the eigenvalues ε_a defined by $H_S|\phi_a\rangle = \varepsilon_a|\phi_a\rangle$ remain constant throughout the rotation.

For single-molecule magnets with half-odd integer spin length, Kramers theorem guarantees that diagonalisation of H_S will always yield a ground state doublet $|\phi_\pm\rangle$ whose instantaneous energy $\varepsilon_+ = \varepsilon_- = \varepsilon_0$ can be harmlessly shifted to zero.[30] As a consequence, ground state degeneracy is maintained throughout any adiabatic rotation and thus triggers the onset of a non-Abelian Berry phase, a unitary transformation producing a linear superposition of the two initial degenerate states. In general this is not the case for integer spin SMMs where the rhombic anisotropy term introduces a tunnel splitting gap between the ground doublet states. We will return to this interesting case in Sections 3.4 and 3.5 but for now, we assume a perfect ground state degeneracy.

2.2 The non-Abelian geometric propagator

Let $\mathscr{M}_0$ represent an N-fold dimensional manifold composed of the subset of instantaneous ground states $|\eta_a(\boldsymbol{\lambda})\rangle$ of a Hamiltonian $H(\boldsymbol{\lambda})$ which remain degenerate throughout a cyclic and adiabatic variation of d classical parameters $\boldsymbol{\lambda} = (\lambda^1, \ldots, \lambda^d)$. For $N \geq 2$, an initial wavefunction prepared within this subspace evolves into linear combinations of states from $\mathscr{M}_0$ according to the Berry phase (see Supplementary Note 1 for a careful derivation, ESI†)

$$U = \mathscr{P}\exp\left(-\oint_\Gamma \mathscr{A}_\mu d\lambda^\mu\right) \quad (2)$$

where $\mathscr{P}$ denotes path ordering, Γ is the cyclic path traced out in d-dimensional parameter space and $\mathscr{A}_\mu d\lambda^\mu$ is the associated non-Abelian gauge potential (here we adopt the Einstein summation convention). The $\mathscr{A}_\mu$'s are $N \times N$ matrices with matrix elements

$$\mathscr{A}_{\mu,ab} = \langle\eta_a(\boldsymbol{\lambda})|\frac{\partial}{\partial\lambda^\mu}|\eta_b(\boldsymbol{\lambda})\rangle \quad (3)$$

between all states of $\mathscr{M}_0$.

In this work, we study the spin dynamics triggered within the degenerate ground manifold, $\mathscr{M}_0$, of nanomagnets undergoing rotations in physical space parametrised by the Euler angles α, β and γ. The non-Abelian gauge potential (derived explicitly in Supplementary Note 2, ESI†) is defined by the infinitesimal line element $\mathscr{A}_\mu d\lambda^\mu = \mathscr{A}_\alpha d\alpha + \mathscr{A}_\beta d\beta + \mathscr{A}_\gamma d\gamma$ where

$$\begin{aligned}\mathscr{A}_\alpha &= i\left(\mathbb{S}_x \sin\beta\cos\gamma - \mathbb{S}_y \sin\beta\sin\gamma - \mathbb{S}_z\cos\beta\right)\\ \mathscr{A}_\beta &= -i\left(\mathbb{S}_x\sin\gamma + \mathbb{S}_y\cos\gamma\right)\\ \mathscr{A}_\gamma &= -i\mathbb{S}_z.\end{aligned} \tag{4}$$

The $\mathbb{S}_i'$s are matrix representations of the angular momentum operators S_i on the basis of the ground spin states of H_S. Unlike in previous studies of rotation-induced spin dynamics,[27,36] we note that the loss of cylindrical symmetry in H_S (owing to the inclusion of rhombic anisotropy) necessitates that the gauge potential $\mathscr{A}_\mu$ be defined in the three-dimensional space spanned by all three Euler angles, rather than just α and β alone.

2.3 Rotations about loops enclosing simply and non-simply connected domains

Although the most general rotation is defined by all three Euler angles discussed at the end of last section, we choose here special closed paths in parameter space that are defined by constant, but generally non-zero, values of γ. In particular, we investigate rotations about two topologically distinct closed loops traced out by rotations on the surface of the unit sphere: (i) square paths Γ_{square} which do not enclose the poles of the sphere and (ii) circular paths Γ_{circle} which do. Examples of each of these paths are depicted schematically in Fig. 1 as green and purple line segments, respectively. Note that the third Euler angle γ could also be allowed to vary along these paths provided that initial and final coordinate axes vectors $\mathbf{e}_x$, $\mathbf{e}_y$, $\mathbf{e}_z$ coincide on completion of the rotation. This ensures that the macroscopic rotation forms a true closed loop in parameter space.

In the first instance, the geometric propagator U_{square} which takes the system around a closed square path on the unit sphere can, due to path-ordering, be decomposed into the ordered product of geometric propagators $U^{(4)}_{\text{square}}U^{(3)}_{\text{square}}U^{(2)}_{\text{square}}U^{(1)}_{\text{square}}$ along each of the four legs (enumerated in Fig. 1) in which the system is rotated along constant lines of either latitude or longitude. Explicitly, these four propagators are

$$\begin{aligned}U^{(1)}_{\text{square}} &= \mathrm{e}^{-i(\alpha_2-\alpha_1)\left(\mathbb{S}_x\sin\beta_1\cos\gamma-\mathbb{S}_y\sin\beta_1\sin\gamma+\mathbb{S}_z\cos\beta_1\right)}\\ U^{(2)}_{\text{square}} &= \mathrm{e}^{i(\beta_2-\beta_1)\left(\mathbb{S}_x\sin\gamma+\mathbb{S}_y\cos\gamma\right)}\\ U^{(3)}_{\text{square}} &= \mathrm{e}^{i(\alpha_2-\alpha_1)\left(\mathbb{S}_x\sin\beta_2\cos\gamma-\mathbb{S}_y\sin\beta_2\sin\gamma+\mathbb{S}_z\cos\beta_2\right)}\\ U^{(4)}_{\text{square}} &= \mathrm{e}^{-i(\beta_2-\beta_1)\left(\mathbb{S}_x\sin\gamma+\mathbb{S}_y\cos\gamma\right)}.\end{aligned} \tag{5}$$

Provided that $0 \le \alpha_1 \le \alpha_2 < 2\pi$ and $0 < \beta_1 \le \beta_2 < \pi$, the area enclosed by the square path is a simply connected domain on the unit sphere. Thus, it is simple to show that in the limits

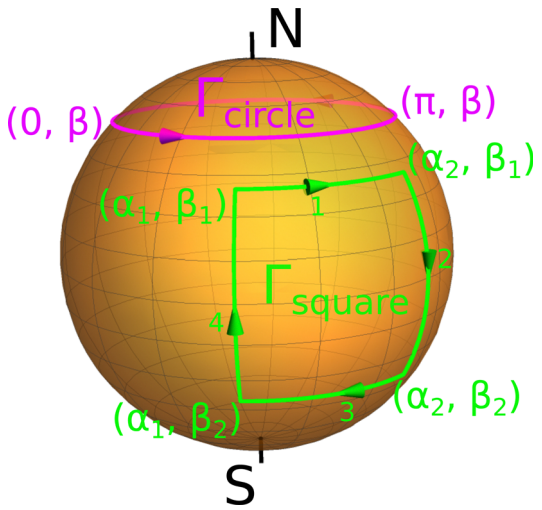

Fig. 1 Rotation paths on the unit sphere. We illustrate the two closed loops of interest, Γ_{square} in green and Γ_{circle} in purple, generated on the unit sphere by rotating the coupled electronic and nuclear spin by the Euler angles α and β. The square path is broken into four segments (labelled in the diagram) in which the coupled system is rotated along either constant lines of longitude or latitude. The circular path Γ_{circle} can be seen to enclose a non-simply connected domain of the sphere, containing either the north or south pole. For both paths, the third Euler angle γ remains constant but, in general, non-zero.

$|\alpha_1 - \alpha_2| \to 0$ and $|\beta_1 - \beta_2| \to 0$, where the square loop is shrunk to an infinitesimally small point, U_{square} approaches the $N \times N$ unit matrix $\mathbb{I}_N$ as intuition dictates.

The circular loop Γ_{circle} does not enclose a simply connected domain of the unit sphere. Consequently, the gauge potential defined in eqn (4) is ill-suited for the calculation of the geometric propagator around these kinds of loops for spins with non-integer ground state magnetic moments.[27] In order to eliminate this pathology it is necessary to make a change of basis using the unitary operator $\rho = \exp(i(\alpha+\gamma)S_z)$, yielding a gauge transformed potential

$$\mathscr{A}'_\nu d\lambda^\nu = \rho^\dagger \mathscr{A}_\mu d\lambda^\mu \rho + \rho^\dagger d\rho \tag{6}$$

which is now well behaved everywhere on the unit sphere except for the south pole. In general, the transformed potential $\mathscr{A}'_\nu$ describes precisely the same physics as $\mathscr{A}_\mu$ (*i.e.* the potential is gauge invariant) provided that the integration path Γ in eqn (2) is closed.[27] While the new potential could in principle make the evaluation of the path-ordered intergal eqn (2) more involved, in practice a slightly modified version of the simpler gauge potential can be used, due to the equivalence

$$\mathscr{P}\exp\left(-\oint_\Gamma \mathscr{A}'_\nu d\lambda^\nu\right) = \rho_{\mathrm{f}}^\dagger \mathscr{P}\exp\left(-\oint_\Gamma \mathscr{A}_\mu d\lambda^\mu\right)\rho_i \tag{7}$$

where ρ_{i} and ρ_{f} are the unitary transformations evaluated at the initial and final points of the loop respectively. The geometric propagator along the circular path thus reads

$$U_{\text{circle}} = \mathrm{e}^{-i(2\pi+\gamma)\mathbb{S}_z}\mathrm{e}^{-2\pi i\left(\mathbb{S}_x\sin\beta\cos\gamma-\mathbb{S}_y\sin\beta\sin\gamma+\mathbb{S}_z\cos\beta\right)}\mathrm{e}^{i\gamma\mathbb{S}_z}. \tag{8}$$

3 Results

3.1 The influence of magnetic anisotropy on non-Abelian dynamics

As a consequence of the anisotropic energy landscape of the SMM spin states caused by the interplay between crystal field interactions and spin–orbit coupling, different paths in parameter space will lead to different dynamical properties. It is therefore intuitive that varying the crystal field parameters D and E (which encapsulate this interplay in our model Hamiltonian H_S) will influence the non-Abelian spin dynamics discussed here. This simple fact could be used either as a design principle for SMMs optimised for desired quantum dynamical applications, or to indirectly probe crystal field Hamiltonians *via* quantum dynamics experiments.

Given that the most easily measurable effect of the quantum dynamical behaviour in SMMs triggered by a non-Abelian geometric phase is a change in the magnetic moment brought about by the modulation of the degenerate ground state amplitudes, in this section we set out to study the effect of D and E on the achievable population transfer dynamics between the degenerate ground states of Kramers-type SMMs. To achieve this we consider rotations about the square path Γ_{square} with $\alpha_1 = 0$, $\alpha_2 = 90^\circ$, $\beta_1 = 60^\circ$ and $\beta_2 = 120^\circ$, and about the circular path Γ_{circle} with $\beta = 90^\circ$. For simplicity, we initially set $\gamma = 0^\circ$ for both rotations. When $\beta = 90^\circ$ and $\gamma = 0^\circ$, the propagator for the great circle (eqn (8)) is

$$U_{\text{circle}} = \begin{pmatrix} e^{-2\pi i M_z}\cos(2\pi M_x) & -ie^{-2\pi i M_z}\sin(2\pi M_x) \\ -ie^{2\pi i M_z}\sin(2\pi M_x) & e^{2\pi i M_z}\cos(2\pi M_x) \end{pmatrix} \quad (9)$$

where $M_x = \langle\phi_-|S_x|\phi_+\rangle$ and $M_z = \langle\phi_+|S_z|\phi_+\rangle$. The propagator for the square path is similarly a 2×2 matrix depending on the matrix elements $\langle\phi_-|S_x|\phi_+\rangle$, $\langle\phi_-|S_y|\phi_+\rangle$ and $\langle\phi_+|S_z|\phi_+\rangle$, though its analytical presentation is rather cumbersome and unenlightening. We assume that prior to rotation, the system is initialised in the $|\phi_+\rangle$ ground state of H_S and, in Fig. 2, we report the squared amplitude of this state after rotation around the square loop (top) and circular loop (bottom).

For both rotation paths shown in Fig. 2, the final composition of the ground doublet wavefunction differs the most from the initialised state when S is small and E is near critical. This trend is intuitive since the non-Abelian dynamics here is triggered by the $\mathbb{S}_x$ and $\mathbb{S}_y$ matrices *via* eqn (5) and (8). For these matrices to be non-zero, the matrix elements $\langle\phi_+|S_\pm|\phi_-\rangle$ (with $S_\pm = S_x \pm iS_y$) must be non-vanishing and hence a portion of $\left|M_S = \pm\frac{1}{2}\right\rangle$ must be recovered in the ground doublet *via* the rhombic anisotropy term in H_S. This condition is most effectively met for small S and large $|E|$.

Interestingly, for the rotation paths chosen here, critical rhombicity does not necessarily lead to maximal population transfer to $|\phi_-\rangle$. Instead, maximal transfer occurs for $S = 3/2$ nanomagnets when $|E/D| \sim 0.2$. It turns out that this value of $|E/D|$ leads to a magnetic moment which maximises the off-diagonal matrix elements of eqn (9) and minimises its diagonal elements. An analogous situation is observed for the propagator of the square loop at around $|E/D| \sim 0.25$.

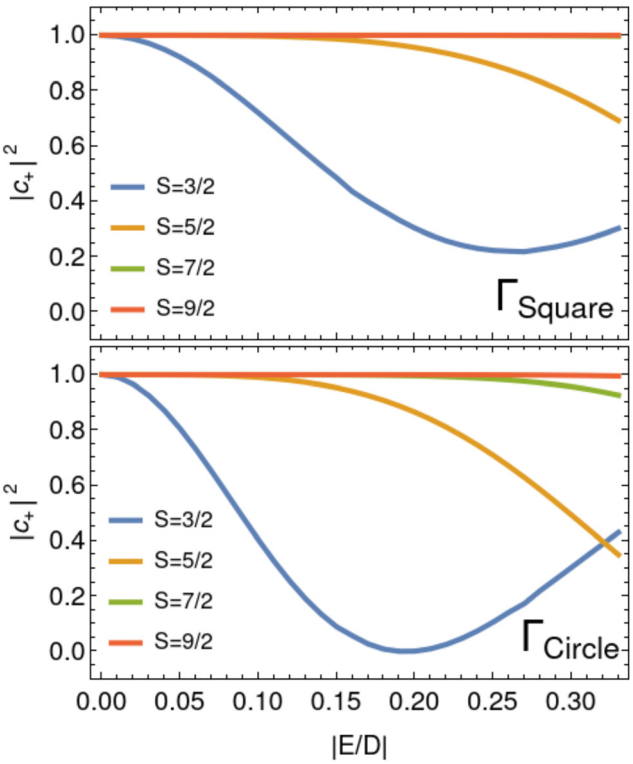

Fig. 2 Squared amplitude $|c_+|^2$ of $|\phi_+\rangle$ as a function of the ratio $|E/D|$ for a range of half-integer spin lengths S, on completion of rotation of the SMM around the square (top) and circular paths (bottom) described in the main text. The system is initialised in the $|\phi_+\rangle$ ground doublet energy eigenstate before rotation.

It is worthwhile noting that we also investigated the role of the γ rotation in determining the final ground state composition of the magnet after rotation about Γ_{square} and Γ_{circle}. While the final amplitudes of all spin systems rotated about Γ_{square} were only imperceptibly changed from those reported in Fig. 2, the choice of γ had some impact on the final wavefunction compositions of the $S = 3/2$, $5/2$ and $7/2$ nanomagnets rotated about the great circle Γ_{circle}. The largest change was observed for $\gamma = 90^\circ$ where population transfer to the $|\phi_-\rangle$ state was maximsed for $S = 5/2$ and $S = 7/2$ at critical rhombicity, and for $S = 3/2$ at $|E/D| \sim 0.15$.

3.2 Towards a holonomic implementation of Grover's algorithm

We now show how this effect can be utilised to construct single-qubit gates, with a mind towards the holonomic implementation of Grover's search algorithm.[39] We follow here an approach to Grover's algorithm proposed by Fahri and Gutman in 1998[40] which does not require the use of quantum oracles. This version of Grover's algorithm has subsequently been employed using resonant microwave pulses delivered to the $I = 3/2$ nuclear qudit of a $TbPc_2$ single-molecule magnet.[16] In that work, two types of quantum gates were demonstrated (i) a single qubit Hadamard gate which prepared the qudit states in a coherent linear

superposition, and (ii) logic gates which selectively populated just one of the four qubit states at a time.

We endeavour to show how these gates could be implemented *via* macroscopic rotations of a recently reported $CoCl_2(tu)_4$ single-molecule magnet[41] using the ground doublet of the $S = 3/2$ spin manifold as a computational basis. A rather good agreement was found between experimental magnetic measurements of $CoCl_2(tu)_4$ and theoretical simulations using the same effective spin Hamiltonian H_S as reported here, with the parameters $D = -63$ cm^{-1} and $|E/D| = 0.22$. We adopt the same values in the following sections.

3.2.1 Single-qubit Hadamard gate. To begin, we assume it possible to initialise the qubit in the $|\phi_+\rangle$ state *via* the application of a small magnetic field for a sufficiently long time; the field is removed before any rotation takes place.[5] Then, a coherent linear superposition of the qubit states (up to a global phase θ) is achieved by applying the Hadamard gate which, in matrix notation is

$$U_{\mathscr{H}} = \frac{e^{i\theta}}{\sqrt{2}}\begin{pmatrix} 1 & 1 \\ 1 & -1 \end{pmatrix}. \quad (10)$$

To implement the Hadamard gate on the initialised qubit, we rotate its magnetic anisotropy axis around the square loop defined in eqn (5) with the Euler angles α_1, α_2, β_1, β_2 and γ obtained from numerical solution of $(U_{\text{square}})_{11} = (U_{\text{square}})_{21}$. The solution space of this equation can be reduced by taking $\alpha_1 = 0$ and fixing the gap $\beta_1 - \beta_2$. We find that rotation about the square loop defined by $\alpha_1 = 0$, $\alpha_2 = 72^\circ$, $\beta_1 = 60^\circ$, $\beta_2 = 120^\circ$ and $\gamma = 87^\circ$, drives the system into the desired coherent linear superposition $e^{i\theta}(|\phi_+\rangle + |\phi_-\rangle)/\sqrt{2}$.

To investigate in what limit adiabaticity is satisfied for the rotation of this particular system, we numerically integrated the time-reduced Schrödinger equation $\partial_s|\psi(s)\rangle = (-iT/\hbar)H(\alpha, \beta, \gamma)|\psi(s)\rangle$ where the Euler angles describing the aforementioned square path have been parameterised by the dimensionless quantity $s = t/T$ ($0 \leq s \leq 1$) with T the total time taken to complete the rotation. In Fig. 3 we show the final amplitudes and relative phases of the ground doublet states as function of rotation duration T. For loops which are completed in $T > 10$ ps the single-qubit Hadamard gate is implemented with little error. This can be attributed to the rather large axial splitting of the system which separates the ground doublet from the first excited doublet by $\Delta E = 135$ cm^{-1}. In this case, $\hbar/\Delta E \approx 5 \times 10^{-14}$ s, so for $T = 10^{-11}$ s, adiabaticity is satisfied and the formalism presented in Section 2.2 is valid.

3.2.2 State specific amplification. Beginning from the coherent linear superposition $e^{i\theta}(|\phi_+\rangle + |\phi_-\rangle)/\sqrt{2}$ obtained from the previous section, we now demonstrate the selective amplification of $|\phi_+\rangle$ and $|\phi_-\rangle$ *via* rotations along the closed square loops $\Gamma_\pm$. In general this is achieved by rotating the qubit along different square paths where the rotation parameters are solutions to the relations $(U_{\text{square}})_{11} = (U_{\text{square}})_{12}$ and $(U_{\text{square}})_{21} = (U_{\text{square}})_{22}$, respectively. We find for our $CoCl_2(tu)_4$ example that rotation about the square paths Γ_+ with $\alpha_1 = 0$, $\alpha_2 = 70^\circ$, $\beta_1 = 60^\circ$, $\beta_2 = 120^\circ$ and $\gamma = 54^\circ$ and the path Γ_- with $\alpha_1 = 0$, $\alpha_2 = 163^\circ$, $\beta_1 = 60^\circ$, $\beta_2 = 120^\circ$ and $\gamma = 124^\circ$ serve to amplify to near unity, the $|\phi_+\rangle$ and $|\phi_-\rangle$ states, respectively.

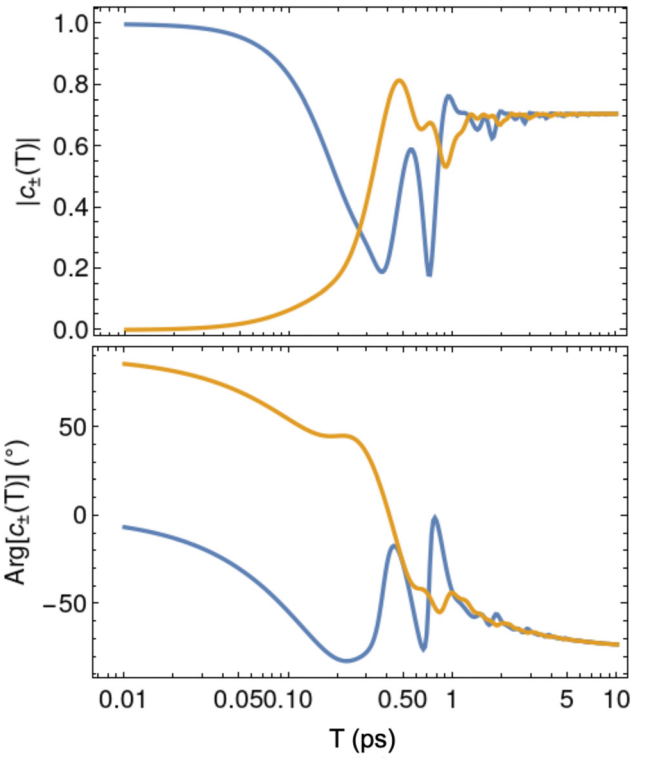

Fig. 3 Final amplitudes (top) and relative phases (bottom) of the ground doublet states of $CoCl_2(tu)_4$ after rotation shown as a function of the rotation duration T. The rotation path was that of a closed square loop with $\alpha_1 = 0$, $\alpha_2 = 72^\circ$, $\beta_1 = 60^\circ$, $\beta_2 = 120^\circ$ and $\gamma = 87^\circ$. The blue and orange curves represent the amplitude/phase of the $|\phi_+\rangle$ and $|\phi_-\rangle$ state respectively. The final wavefunction was obtained from direct numerical integration of Schrödiner's equation with the system initially prepared in the $|\phi_+\rangle$ eigenstate.

We again endeavoured to verify the adiabatic limit implicitly assumed in the above calculations by direct numerical integration of the Schrödinger equation. In Fig. 4, we plot the final amplitudes of the ground doublet states after rotations around the two square paths specified in the previous paragraph. Again, after initialisation with the Hadamard gate from the previous section, with $T \geq 10$ ps, each member of the ground doublet can be selectively populated to near unity, depending on the choice of rotation along either one of the quite different paths.

3.3 Single-ion magnets as quantum gyroscopes

While the non-Abelian geometric propagator formalism developed in Section 2.2 is gauge-invariant only for closed paths in parameter space, macroscopic rotations of nanomagnets along open paths can still lead to a measurable effect provided that the initial state of the system is known *a priori*, *i.e.* the gauge has been fixed by the initial measurement. Monitoring a change in amplitudes of the nanomagnet degenerate ground states can hence provide useful information regarding the orientation of the SMM principal magnetic axis in physical space with respect to a known initial direction.

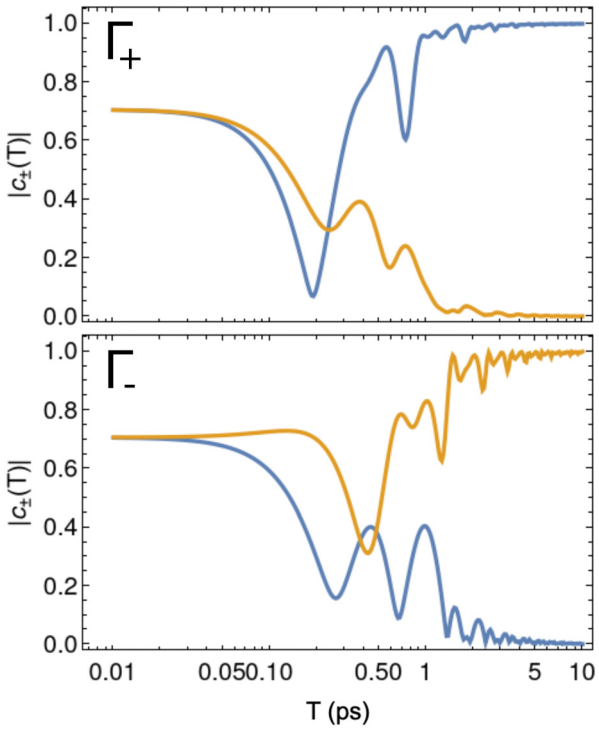

Fig. 4 Final amplitudes of the ground doublet states of $CoCl_2(tu)_4$ after rotation shown as a function of the rotation duration T. The two closed square loops are obtained from eqn (5) with Γ_+: $\alpha_1 = 0$, $\alpha_2 = 70^\circ$, $\beta_1 = 60^\circ$, $\beta_2 = 120^\circ$ and $\gamma = 54^\circ$ and Γ_-: $\alpha_1 = 0$, $\alpha_2 = 163^\circ$, $\beta_1 = 60^\circ$, $\beta_2 = 120^\circ$ and $\gamma = 124^\circ$. The blue and orange curves represent the final populations of the $|\phi_+\rangle$ and $|\phi_-\rangle$ states respectively. The final wavefunction was obtained from direct numerical integration of Schrödiner's equation with the system initially prepared in the coherent superposition $e^{i\theta}(|\phi_+\rangle + |\phi_-\rangle)/\sqrt{2}$ from the previous section.

In Fig. 5 we plot the squared amplitudes of the ground $|\phi_\pm\rangle$ and first excited $|\psi_\pm\rangle$ doublet states of $CoCl_2(tu)_4$ as it undergoes a 360° rotation in the xy-plane obtained from numerical integration of the time-dependent Schrödinger equation with $\alpha = 2\pi t/T$ and $T = 10$ ns. Note that the squared amplitudes of the ground state doublet are essentially single-valued functions of the angle α. Thus, a measurement of the ground state populations at a given time provides information on how far the molecular magnet has rotated from its initial orientation about the global z or "yaw" axis in the lab frame. We repeated this calculation for shorter timescales and found identical results as shown in Fig. 5 up until $T \leq 10$ ps where, from the previous section, adiabaticity begins to breaks down for the particular example of $CoCl_2(tu)_4$. For rotations which occur slower than $T = 10$ ps, the nanomagnet operates as a quantum gyroscope in the xy-plane.

3.4 The case of tunnel-split Ising ground states

For a single-molecule magnet with an integer spin S, small but non-negligible non-axial terms in the crystal field Hamiltonian that can connect the bistable $|\pm S\rangle$ ground states in high-order perturbation theory, lead to a quasi-degenerate tunnelling ground doublet $|\phi_\pm\rangle = (|S\rangle \pm |-S\rangle)/\sqrt{2}$ with tunnel splitting Δ. Assuming that the system is initialised in this quasi-degenerate ground

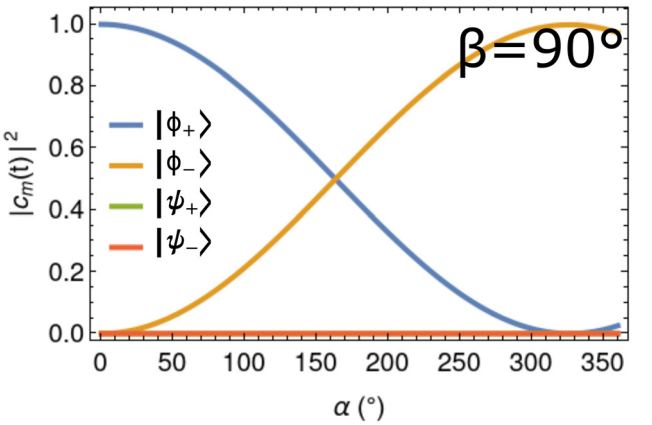

Fig. 5 Squared amplitudes of the ground $|\phi_\pm\rangle$ and first excited $|\psi_\pm\rangle$ Kramers doublets of $CoCl_2(tu)_4$ as it undergoes a 360° rotation in the xy-plane. The squared amplitudes are obtained *via* numerical integration of the Schrödinger equation after initialisation in the $|\phi_+\rangle$ energy eigenstate and then rotation by $\alpha = 2\pi t/T$ for $T = 10$ ns. Here the squared amplitudes correspond to a basis quantised along the rotating anisotropy axis.

manifold and the rotation is not so fast as to activate a dynamics between excited crystal field states, it is possible to write the time-evolution operator of just the quasi-degenerate SMM ground doublet as[42]

$$U(t;t_0) = \mathscr{T}\, e^{-\int_{t_0}^{t} dt'[A(t')+i\Theta]} \tag{11}$$

where the matrix $A(t)$ has elements $A_{ab}(t) = \langle \eta_a(t)|\dot{\eta}_b(t)\rangle$ and the matrix Θ has elements $\Theta_{ab} = \langle \eta_a(t)|H(t)|\eta_b(t)\rangle/\hbar = \varepsilon_a\delta_{ab}/\hbar$ which are time-independent when expressed on the basis of instantaneous eigenstates $|\eta_a(t)\rangle$ of $H(t)$. The integral over time can be converted to a path-ordered integral (see Supplementary Note 1, ESI†) involving the same matrix gauge potential $\mathscr{A}$ as in eqn (3) where λ^μ correspond to the Euler angles α, β and γ. After the system has undergone a complete rotation (when $t = T$) around the circle path Γ_{circle} specified above, the non-adiabatic time evolution operator is

$$\begin{aligned} U_{\text{circle}}^{\text{non-ad}} &= \mathscr{P} e^{-\oint_\Gamma \left(\mathscr{A}_\alpha + i\Theta\frac{dt}{d\alpha}\right)d\alpha + \left(\mathscr{A}_\beta + i\Theta\frac{dt}{d\beta}\right)d\beta + \left(\mathscr{A}_\gamma + i\Theta\frac{dt}{d\gamma}\right)d\gamma} \\ &= e^{-i2\pi\left(\mathbb{S}_x \sin\beta\cos\gamma - \mathbb{S}_y \sin\beta\sin\gamma - \mathbb{S}_z\cos\beta\right) - i\Theta T}. \end{aligned} \tag{12}$$

Within this quasi-degenerate subspace, the $\mathbb{S}_i$ matrices take the simple form $\mathbb{S}_x = \mathbb{S}_y = 0$ and $\mathbb{S}_z = S\sigma_x$ (where σ_x corresponds to the usual Pauli matrix). Accordingly, the propagator in eqn (12) can be expressed analytically as the 2×2 matrix

$$U_{\text{circle}}^{\text{non-ad}} = e^{\frac{-iT\Delta}{2\hbar}} \begin{pmatrix} \cos\frac{\zeta}{2\hbar} + \frac{iT\Delta}{\zeta}\sin\frac{\zeta}{2\hbar} & \frac{4\pi i\hbar S}{\zeta}\cos\beta\sin\frac{\zeta}{2\hbar} \\ \frac{4\pi i\hbar S}{\zeta}\cos\beta\sin\frac{\zeta}{2\hbar} & \cos\frac{\zeta}{2\hbar} - \frac{iT\Delta}{\zeta}\sin\frac{\zeta}{2\hbar} \end{pmatrix} \tag{13}$$

where $\zeta = \hbar\sqrt{8\pi^2S^2(1+\cos 2\beta) + (T\Delta/\hbar)^2}$. Note that owing to the simplicity of the gauge potential for this rotation path, eqn (13) is invariant to γ.

We now show how eqn (13) can act as a single-qubit Hadamard gate, or in other words can create a coherent linear superposition of the qubit computational basis (here the $|\phi_{\pm}\rangle$ quasi-degenerate ground doublet states). Supposing that the nanomagnet is initialised in the ground state $|\phi_{-}\rangle$, then a macroscopic rotation specified by eqn (13) creates a coherent linear superposition of $|\phi_{-}\rangle$ and $|\phi_{+}\rangle$ when β and T are chosen such that

$$\cos\frac{\zeta}{2\hbar}+\frac{iT\Delta}{\zeta}\sin\frac{\zeta}{2\hbar}=\frac{4\pi i\hbar S}{\zeta}\cos\beta\,\sin\frac{\zeta}{2\hbar}. \tag{14}$$

Since the RHS of eqn (14) is purely imaginary, for such a relation to hold we must have that $\cos\zeta/2\hbar = 0$ or equivalently that $\zeta/2\hbar = (2n+1)\pi/2$ for $n \in \mathbb{N}\cup\{0\}$. Using this condition in eqn (14) yields $T = (4\pi S\hbar/\Delta)\cos\beta$, so we find that

$$\frac{\zeta}{2\hbar}=\frac{1}{2}\sqrt{8\pi^2S^2(1+\cos 2\beta)+(T\Delta/\hbar)^2}=\frac{(2n+1)\pi}{2} \tag{15}$$

which results in $\cos\beta = (2n+1)/4\sqrt{2}S$ and consequently $T = (2n+1)\pi\hbar/\sqrt{2}\Delta$. Interestingly, given the spin quantum number S there are several allowed values of canting angle β, and corresponding rotation times T, that will result in a coherent linear superposition of the non-Kramers SMM ground doublet tunnelling states with the condition that n is a whole number and $0 \le n < (4\sqrt{2}S-1)/2$. To maximise the possible choices of rotation speed and canting angle for practical implementations of this effect, molecular magnets with large S spin projections in the quasi-degenerate tunnelling ground states should be favoured.

The above rotation acting on the tunnelling ground state $|\phi_{-}\rangle = (|S\rangle - |-S\rangle)/\sqrt{2}$ is tantamount to the preparation of the SMM in the $|S\rangle$ quantum state. Since we have assumed that S_z does not commute with the nanomagnet Hamiltonian, once the nanomagnet has been prepared in the $|S\rangle$ state by the appropriate macroscopic rotation, a periodic tunnelling of the SMM magnetic moment triggered by the non-axial terms of the crystal field potential, will ensue along its principal magnetic axis taking the maximal values $\mu_z = \pm g\mu_B S$. In a crystal of nanomagnets, the collective in-phase oscillation of each molecular magnetic moment will give rise to an oscillating macroscopic magnetisation that can be readily detected. We note *en passant* that, following a similar line of reasoning as above, the $|-S\rangle$ state can also be prepared from $|\phi_{-}\rangle$ with precisely the same macroscopic rotation but now performed clockwise instead of anticlockwise, or equivalently with $\beta \to \pi - \beta$.

3.5 $TbPc_2$ as a rotating qubit candidate

Results from the previous section suggest that macroscopic rotations of integer spin single-molecule magnets could be employed to realise single-qubit gating operations for a holonomic implementation of Grover's algorithm where the quasi-degenerate ground doublet acts as the two-dimensional computational basis. In parallel with a recent implementation of Grover's algorithm on the nuclear qudit states of the well-known (bis)-phthalocyanine terbium SMM ($TbPc_2$),[16] we demonstrate here how non-adiabatic macroscopic rotations of the same molecule can be utilised to construct logic gates which act instead on the quasi-degenerate 4f tunnelling ground states. In particular, we will demonstrate (i) a single qubit Hadamard gate which prepares the quasi-degenerate ground doublet states into a coherent linear superposition, and subsequently (ii) logic gates which selectively amplify each member of the ground quasi-degenerate doublet beginning from the initialised coherent linear superposition.

The [Xe]$4f^8$ electronic configuration of Tb^{3+} results in an energetically well isolated $^7F_6$ spin–orbit ground multiplet characterised by the $J = 6$ ($S = 3$, $L = 3$) total angular momentum quantum number. The splitting of this multiplet due to the crystal field of the two phthalocyanine ligands which sandwich the Tb^{3+} ion is captured particularly well with the Hamiltonian[43,44]

$$\begin{aligned}H_{TbPc_2} &= \theta_2 A_2^0\langle r^2\rangle O_2^0(\mathbf{J})+\theta_4\left(A_4^0\langle r^4\rangle O_4^0(\mathbf{J})\right.\\ &\left.+A_4^4\langle r^4\rangle O_4^4(\mathbf{J})\right)+\theta_6 A_6^0\langle r^6\rangle O_6^0(\mathbf{J})\end{aligned} \tag{16}$$

where θ_2, θ_4, θ_6 and $O_k^q(\mathbf{J})$ are the well documented Stevens parameters and Stevens operators for Tb^{3+}, respectively.[45] The $A_k^q\langle r^k\rangle$ terms are experimentally determined ligand field parameters which take the values $A_2^0\langle r^2\rangle = 414\ cm^{-1}$, $A_4^0\langle r^4\rangle = -228\ cm^{-1}$, $A_4^4\langle r^4\rangle = 10\ cm^{-1}$ and $A_6^0\langle r^6\rangle = 33\ cm^{-1}$.[46,47] The axial terms in eqn (16) lead to a degenerate $|m_J = \pm 6\rangle$ ground doublet which is thermally well isolated (by $>400\ cm^{-1}$) from all other $|m_J\rangle$ states. The non-axial $\theta_4 A_4^4\langle r^4\rangle O_4^4(\mathbf{J})$ term mixes these states in third order perturbation theory introducing a tunnel splitting $\Delta = 7.29\times 10^{-7}\ cm^{-1}$ and results in the quasi-degenerate tunnelling ground states $|\phi_{\pm}\rangle = (|m_J=-6\rangle \pm |m_J=6\rangle)/\sqrt{2}$.

Using the result from the previous section (with S understood as $J = 6$), n can be chosen as any whole number between $0 \le n \le 16$ resulting in 17 different combinations of β and T that will implement a Hadamard gate on the quasi-degenerate $TbPc_2$ ground doublet. We show each possible path in Fig. 6a but highlight especially the $n = 10$ path which requires a canting angle $\beta = 52^\circ$ and a rotation time of $T = 339\ \mu s$. In principle, one ought to perform the rotation as fast as possible (*i.e.* choose the path corresponding to minimal n) to ensure that decoherent processes such as spin–lattice relaxation do not interfere with the coherent dynamics of the SMM undergoing rotation. We choose to focus on the $n = 10$ path here since the required rotation time is in line with similar experimental setups which have already exposed Berry phase splittings in a rotating $NaClO_3$ crystal[28] as well as measurements of a rapidly rotating diamond qubit.[48,49]

To investigate the coherent dynamics of the quasi-degenerate tunnelling states during rotation as well as to verify the assumptions leading to eqn (13), we numerically integrated the time-dependent Schrödinger equation for the rotating $TbPc_2$ molecule using the Hamiltonian from eqn (16). The resultant amplitudes $|c_{\pm}(t)|$ of the tunnelling states $|\phi_{\pm}\rangle$ are plotted as functions of time t in Fig. 6b in the eigenframe of the rotating $TbPc_2$ quantisation axis as well as the relative phase difference between the $|\phi_{\pm}\rangle$ states in Fig. 6c. Indeed we find that once a single rotation has been completed, a linear superposition of the tunnelled states is prepared from the initial conditions $c_{-}(0) = 1$ and $c_{+}(0) = 0$. Curiously, Fig. 6b and c show that throughout the rotation, the system oscillates eleven times between the $|\phi_{-}\rangle$ tunnelling eigenstate and the linear

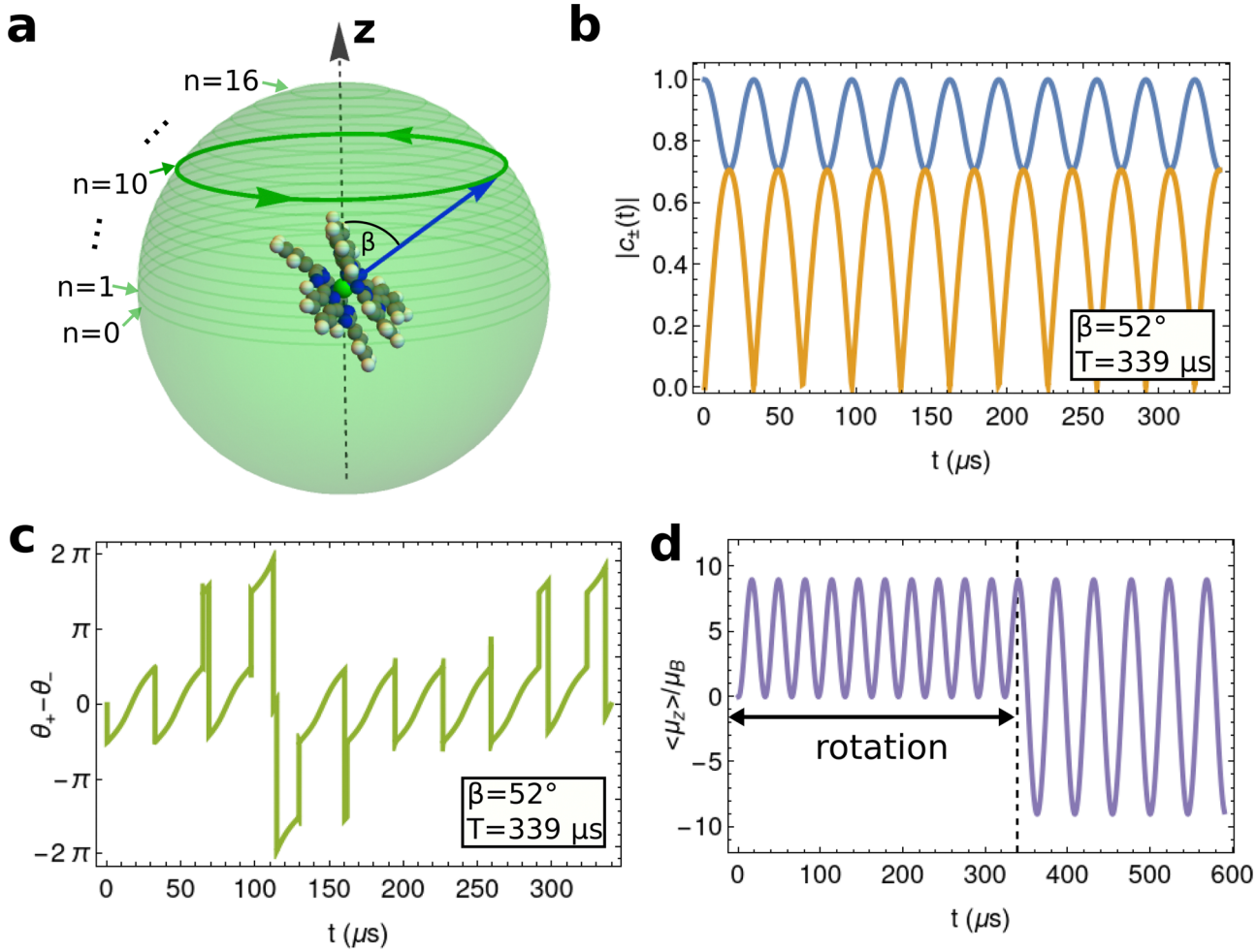

Fig. 6 Hadamard gate implementation through the non-adiabatic macroscopic rotation of a $TbPc_2$ single-molecule magnet. (a) Schematic depiction of the rotation path (dark green loop) of the $TbPc_2$ quantisation axis (blue arrow) about the lab-frame z axis (black dashed arrow) when $n = 10$. Other possible paths are shown as translucent green loops and a select few are labelled. (b) Populations of the quasi-degenerate ground doublet states of $TbPc_2$ (c_- in blue and c_+ in yellow) undergoing the rotation specified in (a). (c) Phase difference between the quasi-degenerate ground doublet states of $TbPc_2$ as it undergoes the rotation specified in (a). (d) Time evolution of the $TbPc_2$ magnetic moment as it undergoes the rotation specified in (a) up until $T = 339$ μs (dashed line). For $t > 339$ μs the SMM quantisation axis remains stationary and the magnetic moment tunnels between $-9\mu_B$ and $9\mu_B$ solely due to the non-axial crystal field. The amplitudes, phase difference and magnetic moment plotted in (b)–(d) were obtained from numerical integration of the Schödinger equation over the full Hilbert space of the Tb^{3+} ground $^7F_6$ ground multiplet and are plotted in the eigenframe of the rotating SMM.

superposition $e^{i\chi}(|\phi_-\rangle + |\phi_+\rangle)/\sqrt{2}$ (including some global phase χ). We also checked all other combinations of β and T within the range $0 \leq n \leq 16$ using the same numerical integration procedure and found consistently that the $TbPc_2$ system undergoes $n + 1$ oscillations between $|\phi_-\rangle$ and $(|\phi_-\rangle + |\phi_+\rangle)/\sqrt{2}$ during each rotation.

In Fig. 6d we plot the time-evolution of the $TbPc_2$ magnetic moment as the SMM undergoes the cyclic macroscopic rotation corresponding to $n = 10$ (0 μs $\leq t \leq 339$ μs) and is then left stationary (339 μs $< t \leq 600$ μs). During rotation, Fig. 6b shows clearly that the $TbPc_2$ wavefunction oscillates between $|\phi_-\rangle$ and the coherent linear superposition corresponding to $|m_J = 6\rangle$. Naturally, the $TbPc_2$ magnetic moment oscillates between $\mu_z = 0$ and its maximal value $\mu_z = 6g_J\mu_B$ ($g_J = 4/3$) during this time as well. After the rotation is completed (*i.e.* the Hadamard gate has been executed) the $TbPc_2$ molecule is prepared in the $|m_J = 6\rangle$ state which is *not* an energy eigenstate of Hamiltonian (16) due to the $\theta_4 A_4^4 \langle r^4 \rangle O_4^4(\mathbf{J})$ non-axial term. As a result, the nanomagnet tunnels between $|m_J = 6\rangle$ and $|m_J = -6\rangle$ angular momentum states and thus the magnetic moment oscillates from $\mu_z = 6g_J\mu_B$ to $\mu_z = -6g_J\mu_B$ accordingly. Notably, from our proof-of-concept model above we have assumed a perfect D_{4d} symmetry of the $TbPc_2$ crystal field and have neglected hyperfine coupling between the $TbPc_2$ electronic spin and its $I = 3/2$ nuclear spin. With some minor alterations to the experimental protocol, we show in Supplementary Note 4 (ESI†) that this effect persists regardless of crystal field symmetry lowering and hyperfine coupling.

Finally we note that for a given β, T pair specified by n, the same rotation can be performed to amplify the $|\phi_-\rangle$ energy eigenstate to unity from the linear combination $(|\phi_-\rangle + |\phi_+\rangle)/\sqrt{2}$. The $|\phi_+\rangle$ state can also be amplified to unity by rotating the quantisation axis

along the same path but now clockwise instead of anticlockwise (*i.e.* with the substitution $\beta \rightarrow \pi - \beta$).

3.6 Rotation time and angle deviations

We have so far considered idealised rotation paths and times without concern for errors introduced by experimental/instrumental uncertainties. We use the $n = 10$ rotation path of the $TbPc_2$ single-molecule magnet described in the last section as a test case to investigate the effect of rotation time and path fluctuation errors on the holonomic implementation of a Hadamard gate on a single-molecule magnet.

For the perfect canting angle β and rotation time T, the action of the Hadamard gate should result in equal populations and phases of the tunnelled $TbPc_2$ ground doublet states. In Fig. 7a we show the difference in these populations $\Delta c(T + \Delta T) = |c_+(T + \Delta T)| - |c_-(T + \Delta T)|$ and relative phases $\Delta\theta(T + \Delta T) = \theta_+(T + \Delta T) - \theta_-(T + \Delta T)$ (mod 2π) at the end of the rotation, due to under/over rotation by a time ΔT. The error in the populations $\Delta c(T + \Delta T)$, grows approximately quadratically with the over/under rotation time ΔT, leading to almost a complete annulment of the Hadamard gate for $|\Delta T/T| \sim 10\%$. The phase error does not grow as rapidly but reaches a maximum of $\pi/2$ when $|\Delta T/T| \sim 10\%$.

To approximate the effect of stochastic fluctuations in the rotation path we obtain the mean values of $\Delta c(T)$ and $\Delta\theta(T)$ from 500 simulations of the $TbPc_2$ rotation described above whereby the Schrödinger equation is numerically integrated up until $T = 339$ μs. For each of these rotations we pseudo-randomly vary the canting angle β throughout the rotation path by drawing from a normal distribution with mean value 52° and standard deviation σ. Typical fluctuations in the β Euler angle for fixed σ during the $TbPc_2$ rotation are plotted in Note S5 (ESI†). For reference, standard deviations of $\sigma = 0.5$ lead to fluctuations in the β canting angle of $\sim 2°$. In Fig. 7b we show the mean values of $\Delta c(T)$ and $\Delta\theta(T)$ as function of the standard deviation σ. Stochastic path fluctuations begin to reduce the fidelity of the Hadamard gate when the β Euler angle fluctuates $>2°$.

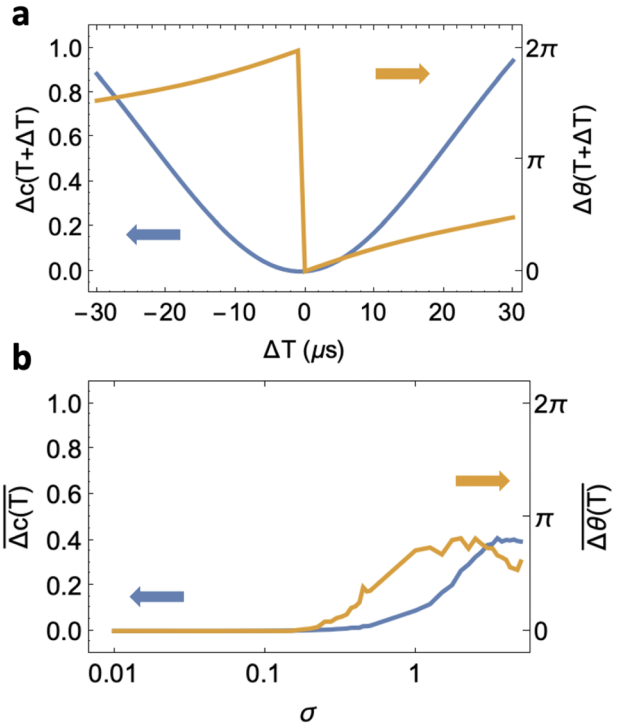

Fig. 7 Quantifying the Hadamard gate errors associated with rotation time and path fluctuations. (a) Difference between the populations (blue) and relative phases (yellow) of the $TbPc_2$ tunnelled ground doublet states after the cyclic rotation described in Section 3.5 with total rotation time $T + \Delta T$. (b) Average difference between the populations (blue) and relative phases (yellow) from 500 simulations of the $TbPc_2$ rotation with a stochastically fluctuating canting Euler angle β. The fluctuations are drawn from a normal distribution centred at 52° with standard deviation σ.

4 Discussion

While we have focused on the specific examples of $CoCl_2(tu)_4$ and $TbPc_2$ single-molecule magnets, there are a myriad of alternative candidate molecules reported in the literature which may also show these effects. For example, the tunnel split $|J = 8, m_J = \pm 8\rangle$ ground doublet of a recently reported Ho^{3+} single-molecule magnet synthesised and characterised by Wu *et al.*[50] In that study, a tunnel splitting of 10^{-5} cm^{-1} was obtained from *ab initio* calculations suggesting that rotations should be carried out on μs timescales to observe the above non-adiabatic rotation-induced spin dynamics of the tunnelling ground states. A further example is a recently reported Ni^{2+} field-induced single-molecule magnet synthesised and characterised by Miklovic *et al.*[51] In that work, excellent agreement between experimental results and simulations was afforded using the $S = 1$ effective spin Hamiltonian $H = DS_z^2 + E(S_x^2 - S_y^2)$ with $D = -13.7$ cm^{-1} and $E = 0.07$ cm^{-1}. The rhombic magnetic anisotropy term resulted in a zero-field tunnelling ground doublet with splitting $\Delta = 0.14$ cm^{-1}. To observe a rotation-induced coherent dynamics between the tunnel split ground doublet states for such a large Δ, would require rotations to be performed with $T < 50$ ns which is several orders of magnitude faster than conventional set-ups so far reported in the literature.[28,48,49] Nevertheless, more sophisticated molecular rotor systems may in the future be leveraged to achieve such rapid, constrained rotations.[52]

We note in addition, that our theoretical model has not accounted for population transfer between the energy eigenstates of H_S mediated by incoherent transitions from the local environment. These could result from lattice phonon-mediated spin transitions in the nanomagnet,[37] stray fields from a bath of nuclear dipoles[53] or potentially from continuous electrical measurement if the SMM can be realised in a spintronics device.[54,55] While we haven't treated these effects directly, we note that for both explicit examples, the quantum logic gating and gyroscopic applications were based on macroscopic rotations that could be performed on timescales much faster than typical incoherent processes (for example the spin relaxation between $TbPc_2$ doublet states has been measured $T_1 \sim 10$ s),[54] thus reducing the risk for spurious, incoherent population transfer.

While the prototypical results presented in this manuscript represent a first step towards the holonomic implementation of Grover's algorithm using macroscopically rotating single-molecule magnets, since the rotation-induced coherent dynamics is confined to the SMM ground doublet, one is restricted to only ever searching a database of two objects. The database might be expanded however, by the extension of the computational basis to include hyperfine states of the SMM. In addition, the macroscopic rotation of different species of SMM confined to the same unit cell could also offer a way to grow the computational basis for a useful holonomic implementation of Grover's algorithm. The explicit discussion of these more complicated scenarios is beyond the scope of this work and will be considered in a future publication.

5 Conclusions

With a theoretical model, we have demonstrated that a spin dynamics can be triggered in the ground doublet of both half-odd integer and integer spin SMMs by macroscopic rotations of its principal magnetic axis.

For half-odd integer spin SMMs, we explored how the crystal field parameters of an effective spin Hamiltonian influence the spin dynamics of the ground Kramers doublet *via* an emergent non-Abelian gauge potential that arises due to the electronic spin adiabatically following the rotating crystal field. As well as an unconventional probe of the spin Hamiltonian parameters, we suggested how this might be utilised to realise holonomic single-qubit quantum logic gates in a $CoCl_2(tu)_4$ single-molecule magnet. Direct numerical integration of Schrödinger's equation revealed that the holonomic gating operations required for such an implementation could be executed on picosecond timescales, orders of magnitude faster than typical spin–lattice relaxation mechanisms. In addition, we demonstrated how this effect could be utilised for a quantum gyroscope inertial sensor based on $CoCl_2(tu)_4$. Again, provided that the rotation speed does not exceed 10 ps, the ground doublet squared amplitudes remain single-valued for rotations in the *xy*-plane and thus their measurement provides direct information about the rotation of the SMM principal magnetic axes.

By lifting the stringent condition that rotations proceed adiabatically, we recovered a tunable non-Abelian spin dynamics in the tunnelling ground (pseudo) doublet of an otherwise general integer spin SMM. We showed that when the quantisation axis is canted by an angle $\beta = \arccos[(2n+1)/4\sqrt{2}S]$ from the lab-frame z axis and rotated along a circular path on the unit sphere for a duration $T = (2n+1)\pi\hbar/\sqrt{2}\Delta$ (with n a whole number between 0 and $(4\sqrt{2}S-1)/2$), the rotation prepares the SMM in a coherent linear superposition of the quasi-degenerate ground doublet states, effectively acting as a single-qubit Hadamard gate. We made a specific example of the well-known single-molecule magnet $TbPc_2$ and showed how this effect could be observed with state-of-the-art set-ups from the current literature. *Via* numerical integration of Schrödinger's equation, we vindicated the approximations implicit in our non-adiabatic geometric propagator approach and exposed a curious $n+1$ oscillation effect in the coherent dynamics of the rotating $TbPc_2$ magnetic moment. We used this prototypical example to explore the effects of rotation time and path fluctuations on the fidelity of a Hadamard gate induced by an SMM macroscopic rotation.

Author contributions

Both authors contributed equally to this work.

Conflicts of interest

There are no conflicts to declare.

Notes and references

1 R. Sessoli, H. L. Tsai, A. R. Schake, S. Wang, J. B. Vincent, K. Folting, D. Gatteschi, G. Christou and D. N. Hendrickson, *J. Am. Chem. Soc.*, 1993, **115**, 1804–1816.
2 M. Mannini, F. Pineider, P. Sainctavit, C. Danieli, E. Otero, C. Sciancalepore, A. M. Talarico, M.-A. Arrio, A. Cornia, D. Gatteschi and R. Sessoli, *Nat. Mater.*, 2009, **8**, 194–197.
3 K. Katoh, H. Isshiki, T. Komeda and M. Yamashita, *Chem. Asian J.*, 2012, **7**, 1154–1169.
4 D. Ray, M. S. Oakley, A. Sarkar, X. Bai and L. Gagliardi, *Inorg. Chem.*, 2023, **62**, 1642–1658.
5 M. N. Leuenberger and D. Loss, *Nature*, 2001, **410**, 789–793.
6 B. Zhou, R. Tao, S.-Q. Shen and J.-Q. Liang, *Phys. Rev. A*, 2002, **66**, 010301.
7 J. Lehmann, A. Gaita-Arino, E. Coronado and D. Loss, *J. Mater. Chem.*, 2009, **19**, 1672–1677.
8 K. Hymas and A. Soncini, *Phys. Rev. B*, 2019, **99**, 245404.
9 A. Lunghi and S. Sanvito, *Nat. Rev. Chem.*, 2022, 1–21.
10 M. N. Leuenberger and D. Loss, *Phys. Rev. B: Condens. Matter Mater. Phys.*, 2001, **63**, 054414.
11 L. Lecren, W. Wernsdorfer, Y.-G. Li, O. Roubeau, H. Miyasaka and R. Clérac, *J. Am. Chem. Soc.*, 2005, **127**, 11311–11317.
12 R. Schenker, M. N. Leuenberger, G. Chaboussant, D. Loss and H. U. Güdel, *Phys. Rev. B: Condens. Matter Mater. Phys.*, 2005, **72**, 184403.
13 L. Escalera-Moreno, N. Suaud, A. Gaita-Arino and E. Coronado, *J. Phys. Chem. Lett.*, 2017, **8**, 1695–1700.
14 K. Irländer and J. Schnack, *Phys. Rev. B*, 2020, **102**, 054407.
15 S. Bertaina, S. Gambarelli, T. Mitra, B. Tsukerblat, A. Müller and B. Barbara, *Nature*, 2008, **453**, 203–206.
16 C. Godfrin, A. Ferhat, R. Ballou, S. Klyatskaya, M. Ruben, W. Wernsdorfer and F. Balestro, *Phys. Rev. Lett.*, 2017, **119**, 187702.
17 R. Hussain, G. Allodi, A. Chiesa, E. Garlatti, D. Mitcov, A. Konstantatos, K. S. Pedersen, R. De Renzi, S. Piligkos and S. Carretta, *J. Am. Chem. Soc.*, 2018, **140**, 9814–9818.
18 A. Ardavan, A. M. Bowen, A. Fernandez, A. J. Fielding, D. Kaminski, F. Moro, C. A. Muryn, M. D. Wise, A. Ruggi, E. J. L. McInnes, K. Severin, G. A. Timco, C. R. Timmel, F. Tuna, G. F. S. Whitehead and R. E. P. Winpenny, *npj Quantum Information*, 2015, **1**, 1–7.

19 K. S. Pedersen, A.-M. Ariciu, S. McAdams, H. Weihe, J. Bendix, F. Tuna and S. Piligkos, *J. Am. Chem. Soc.*, 2016, **138**, 5801–5804.
20 S. Thiele, F. Balestro, R. Ballou, S. Klyatskaya, M. Ruben and W. Wernsdorfer, *Science*, 2014, **344**, 1135–1138.
21 D. Aguila, L. A. Barrios, V. Velasco, O. Roubeau, A. Repollés, P. J. Alonso, J. Sesé, S. J. Teat, F. Luis and G. Arom, *J. Am. Chem. Soc.*, 2014, **136**, 14215–14222.
22 G. A. Timco, S. Carretta, F. Troiani, F. Tuna, R. J. Pritchard, C. A. Muryn, E. J. McInnes, A. Ghirri, A. Candini, P. Santini, G. Amoretti, M. Affronte and R. E. P. Winpenny, *Nat. Nanotechnol.*, 2009, **4**, 173–178.
23 J. Ferrando-Soria, E. Moreno Pineda, A. Chiesa, A. Fernandez, S. A. Magee, S. Carretta, P. Santini, I. J. Vitorica-Yrezabal, F. Tuna, G. A. Timco, E. J. L. McInnes and R. E. P. Winpenny, *Nat. Commun.*, 2016, **7**, 1–10.
24 D. Ranieri, F. Santanni, A. Privitera, A. Albino, E. Salvadori, M. Chiesa, F. Totti, L. Sorace and R. Sessoli, *Chem. Sci.*, 2023, **14**, 61–69.
25 F. Wilczek and A. Zee, *Phys. Rev. Lett.*, 1984, **52**, 2111.
26 P. Zanardi and M. Rasetti, *Phys. Lett. A*, 1999, **264**, 94–99.
27 A. Zee, *Phys. Rev. A*, 1988, **38**, 1.
28 R. Tycko, *Phys. Rev. Lett.*, 1987, **58**, 2281.
29 L.-X. Yu, G. Chen and J.-Q. Liang, *Commun. Theor. Phys.*, 2011, **56**, 382.
30 Y. Liu, A. Roy and M. Stone, *J. Phys. A: Math. Theor.*, 2012, **45**, 135304.
31 V. A. Mousolou, C. M. Canali and E. Sjöqvist, *New J. Phys.*, 2014, **16**, 013029.
32 D. Maclaurin, M. Doherty, L. Hollenberg and A. Martin, *Phys. Rev. Lett.*, 2012, **108**, 240403.
33 S. Arroyo-Camejo, A. Lazariev, S. W. Hell and G. Balasubramanian, *Nat. Commun.*, 2014, **5**, 1–5.
34 K. Nagata, K. Kuramitani, Y. Sekiguchi and H. Kosaka, *Nat. Commun.*, 2018, **9**, 1–10.
35 A. A. Wood, L. C. Hollenberg, R. E. Scholten and A. M. Martin, *Phys. Rev. Lett.*, 2020, **124**, 020401.
36 M. A. Kowarsky, L. C. Hollenberg and A. M. Martin, *Phys. Rev. A*, 2014, **90**, 042116.
37 D. Gatteschi, R. Sessoli and J. Villain, *Molecular nanomagnets*, Oxford University Press on Demand, 2006, vol. 5.
38 J. J. Sakurai and E. D. Commins, *Modern quantum mechanics*, revised edition, 1995.
39 L. K. Grover, *Phys. Rev. Lett.*, 1997, **79**, 4709.
40 E. Farhi and S. Gutmann, *Phys. Rev. A*, 1998, **57**, 2403.
41 S. Tripathi, S. Vaidya, N. Ahmed, E. A. Klahn, H. Cao, L. Spillecke, C. Koo, S. Spachmann, R. Klingeler, G. Rajaraman and M. Shanmugan, *Cell Rep. Phys. Sci.*, 2021, **2**, 100404.
42 J. Anandan, *Phys. Lett. A*, 1988, **133**, 171–175.
43 M. Ganzhorn, S. Klyatskaya, M. Ruben and W. Wernsdorfer, *Nat. Nanotechnol.*, 2013, **8**, 165–169.
44 K. Hymas and A. Soncini, *Phys. Rev. B*, 2020, **102**, 125310.
45 A. Abragam and B. Bleaney, *Electron paramagnetic resonance of transition ions*, Oxford University Press, 2012.
46 N. Ishikawa, T. Iino and Y. Kaizu, *J. Phys. Chem. A*, 2002, **106**, 9543–9550.
47 N. Ishikawa, M. Sugita and W. Wernsdorfer, *Angew. Chem., Int. Ed.*, 2005, **44**, 2931–2935.
48 A. A. Wood, E. Lilette, Y. Y. Fein, N. Tomek, L. P. McGuinness, L. C. Hollenberg, R. E. Scholten and A. M. Martin, *Science Adv.*, 2018, **4**, eaar7691.
49 A. A. Wood, R. M. Goldblatt, R. E. Scholten and A. M. Martin, *Phys. Rev. Res.*, 2021, **3**, 043174.
50 S.-G. Wu, Z.-Y. Ruan, G.-Z. Huang, J.-Y. Zheng, V. Vieru, G. Taran, J. Wang, Y.-C. Chen, J.-L. Liu, L. F. Chibotaru, W. Wernsdorfer, X.-M. Chen and M.-L. Tong, *Chem*, 2021, **7**, 982–992.
51 J. Miklovič, D. Valigura, R. Boča and J. Titiš, *Dalton Trans.*, 2015, **44**, 12484–12487.
52 T. Matsuno, S. Terasaki, K. Kogashi, R. Katsuno and H. Isobe, *Nat. Commun.*, 2021, **12**, 1–7.
53 F. Delgado and J. Fernández-Rossier, *Prog. Surf. Sci.*, 2017, **92**, 40–82.
54 F. Troiani, C. Godfrin, S. Thiele, F. Balestro, W. Wernsdorfer, S. Klyatskaya, M. Ruben and M. Affronte, *Phys. Rev. Lett.*, 2017, **118**, 257701.
55 K. Hymas and A. Soncini, *Phys. Rev. B*, 2021, **104**, 205306.